Nanoscale Research Letters

NANO EXPRESS Open Access

Photo-Fenton Degradation of AO7 and Photocatalytic Reduction of Cr(VI) over CQD-Decorated $BiFeO_3$ Nanoparticles Under Visible and NIR Light Irradiation

Tao Xian[1*], Lijing Di[1], Xiaofeng Sun[1], Hongqin Li[1], Yongjie Zhou[1] and Hua Yang[2]

Abstract

In this work, the carbon quantum dot (CQD)–decorated $BiFeO_3$ nanoparticle photocatalysts were prepared by a hydrothermal method. The TEM observation and XPS characterization indicate that the CQDs are well anchored on the surface of $BiFeO_3$ nanoparticles. Acid orange 7 (AO7) and hexavalent chromium (Cr(VI)) were chosen as the model pollutants to investigate the photocatalytic/photo-Fenton degradation and photocatalytic reduction performances of the as-prepared CQD/$BiFeO_3$ composites under visible and near-infrared (NIR) light irradiation. Compared with bare $BiFeO_3$ nanoparticles, the CQD/$BiFeO_3$ composites exhibit significantly improved photocatalytic and photo-Fenton catalytic activities. Moreover, the composites possess good catalytic stability. The efficient photogenerated charges separation in the composites was demonstrated by the photocurrent response and electrochemical impedance spectroscopy (EIS) measurements. The main active species involved in the catalytic degradation reaction were clarified by radicals trapping and detection experiments. The underlying photocatalytic and photo-Fenton mechanisms are systematically investigated and discussed.

Keywords: $BiFeO_3$ nanoparticles, Carbon quantum dots, CQD/$BiFeO_3$ composites, Photocatalysis

Background

In recent decades, wastewater containing heavy metal ions and organic compounds brings serious damages for environment and human beings. As one of common heavy metal ions, hexavalent chromium (Cr(VI)) derived from electroplating, leather tanning, and printing poses a serious threat for our health owing to its high toxicity [1]. On the other hand, most of organic pollutants (such as dyes) are also toxic and non-biodegradable, which destroy our living environment [2]. Up to now, many techniques have been developed to eliminate organic pollutants and reduce Cr(VI) to Cr(III) [3–5]. Among these methods, photocatalytic and photo-Fenton-like catalytic techniques are regarded to be the promising methods for efficient degradation of organic contaminants and Cr(VI) reduction in wastewater because of their inexpensive cost, non-selectivity, and simplicity of operation [6–9]. The basic steps involved in a photocatalytic degradation process can be described as follows: excitation of photocatalysts, separation and migration of the photogenerated charges, generation of active species on the surface of catalysts, and decomposition of organic compound as well as reduction of Cr(VI) caused by the redox reaction of active species and photo-induced charges [10, 11]. The photo-Fenton-like catalytic reaction is based on the synergistic effects of the Fenton reaction and photocatalytic process. The generation of active species during the Fenton reaction process can be promoted after the introduction of suitable light irradiation, which leads to improved catalytic activity [12, 13]. However, the wide application of photocatalytic and photo-Fenton-like catalytic techniques is limited due to the large bandgap of photocatalysts only responding to UV light (which accounts for ~ 5% of sunlight energy) and their low charge separation efficiency [14]. Generally, it is known that the visible light and near-infrared

* Correspondence: xiantao1985@126.com
[1]College of Physics and Electronic Information Engineering, Qinghai Normal University, Xining 810008, China
Full list of author information is available at the end of the article

(NIR) light occupy ~ 45% and ~ 46% of solar energy, respectively, and their application has received a great deal of interest [15, 16]. As a result, the development of broad spectrum (UV-vis-NIR) active catalysts with efficient separation of photogenerated charges is very important for their practical applications [17–20]. Up to now, the iron-contained catalysts with narrow bandgap are considered as ideal candidates in the photocatalytic and photo-Fenton-like catalytic applications [21–25].

As one of typical iron-contained catalysts, $BiFeO_3$ with perovskite-type structure is known to be an interesting visible light-driven photocatalytic and photo-Fenton-like catalytic material for the degradation of dyes [26–34]. Nevertheless, its catalytic activity is not so strong to meet the application requirements owing to the high recombination rate of photogenerated charges. Moreover, the light response range of $BiFeO_3$ needs to be further extended to NIR light region for effective utilization of sunlight energy. Therefore, many strategies have been used to overcome these shortcomings [35–40].

Carbon quantum dots (CQDs), as an important class of zero-dimensional nanocarbon material, have attracted considerable attentions due to its distinct properties, such as large surface area, low toxicity, high biocompatibility, good water solubility, high chemical stability, good electrical conductivity, and excellent optical properties [41–44]. These prominent properties make it a promising candidate for the practical application in different fields [41–44]. More importantly, the photoexcited CQDs are demonstrated to be an excellent electron donors and acceptors to promote the separation of photogenerated charges in photocatalysts [45]. On the other hand, CQDs are found to be an unique up-converted photoluminescence material, which allows the generation of short-wavelength emission light (from 450 to 750 nm) by the excitation of long-wavelength light (NIR light, from 700 to 1000 nm) [42, 44]. The up-converted emission light can be employed as the excitation light for the production of photogenerated charges in the semiconductors, which extends their light response region [45]. As a result, incorporation of CQDs with photocatalysts is demonstrated to be a promising way to form excellent hybrid composite photocatalysts [46–52]. Chen et al. prepared CQD/$BiFeO_3$ nanocomposites and found their enhanced visible light photocatalytic activity for the dye degradation [53]. To the best of our knowledge, however, there is no work devoted to the photo-Fenton dye degradation and photocatalytic Cr(VI) reduction performances of CQD/$BiFeO_3$ composite photocatalysts under visible or NIR light irradiation.

In this work, the CQD/$BiFeO_3$ composite photocatalysts were prepared by a hydrothermal route. Their photocatalytic and photo-Fenton-like catalytic performance for acid orange 7 (AO7) degradation as well as photocatalytic Cr(VI) reduction activity under visible and NIR light irradiation were systematically investigated. The corresponding catalytic mechanism was proposed.

Methods

Preparation of CQDs

The CQDs were prepared by a hydrothermal method [54]. Glucose (1 g) was added into distilled water (80 ml) under magnetic stirring and ultrasonic treatment to obtain a homogeneous solution. Subsequently, this solution was transferred into a 100-mL Teflon-lined stainless steel autoclave and heated at180 °C for 4 h. After the reaction, the resultant solution was filtered by filter paper twice, and then, the reddish-brown CQDs suspension was obtained.

Fabrication of CQD/$BiFeO_3$ Composites

$BiFeO_3$ nanoparticles were prepared through a polyacrylamide gel route as reported in the literature [55]. The CQD/$BiFeO_3$ composites were fabricated as follows (Fig. 1): $BiFeO_3$ nanoparticles (0.1 g) were introduced into distilled water (70 ml), followed by ultrasonic treatment for 0.5 h to obtain uniform suspension. After that, a certain amount of CQD suspension was added drop by drop into the $BiFeO_3$ suspension under magnetic stirring. The mixture was

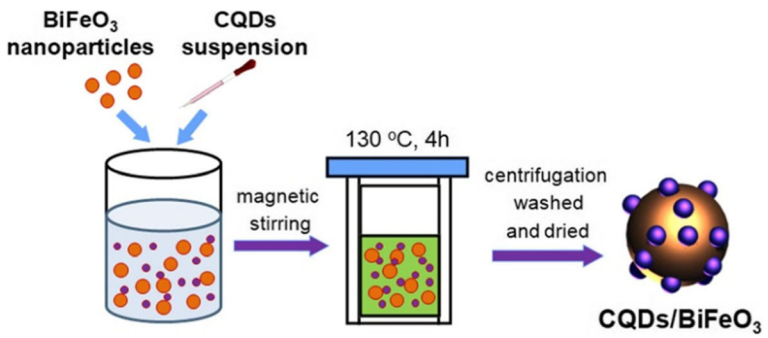

Fig. 1 The schematic illustration of preparation process for CQDs/$BiFeO_3$ composite

moved into the Teflon-lined stainless steel autoclave (100 ml) and heated at130 °C for 4 h. Finally, the product was collected by centrifugation, washed with deionized water, and dried at 60 °C for 8 h. To explore the impact of the CQDs content on the catalytic actives of the composites, a series of CQD/$BiFeO_3$ composites with different mass contents of CQDs were prepared by adding different volumes of CQDs suspension (3, 6, 12, and 24 ml). These composites were correspondingly named as 3C/BFO, 6C/BFO, 12C/BFO, and 24C/BFO.

Photo-Fenton Catalytic and Photocatalytic Degradation of Dye

The photo-Fenton catalytic performance of the as-prepared CQD/$BiFeO_3$ composites was investigated toward the degradation of AO7 separately irradiated by visible light (300-W xenon lamp with a 420-nm cutoff filter) and NIR light (300-W xenon lamp with a 800-nm cutoff filter). In a typical experiment, the photocatalyst (0.1 g) was placed into AO7 solution (200 ml, 5 mg/L), and magnetically stirred in dark for 0.5 h to achieve a adsorption-desorption equilibrium between the photocatalyst and AO7 molecules. Subsequently, a certain amount of H_2O_2 solution was added into the suspension, and the xenon lamp was turned on to start the catalytic reaction. In the catalytic process, a small amount of the reaction solution (2 ml) was taken and centrifuged to eliminate the catalyst. The absorbance of the supernatant was measured by a UV-vis spectrophotometer at 484 nm to obtain the AO7 concentration. On the other hand, the photocatalytic degradation of AO7 over the samples was performed to evaluate their photocatalytic activities under the same conditions in the absence of H_2O_2.

The recycling catalytic experiments were carried out to test the catalytic reusability of the samples. After the first catalytic experiment, the catalyst was separated from the solution by centrifugation, washed with deionized water, and dried. The collected catalyst was added into the new dye solution for the next catalytic reaction with the same condition.

To confirm the reactive species involved in the photocatalytic and photo-Fenton catalytic degradation processes, the active species trapping experiments were performed by adding several scavengers under the same conditions as mentioned above. Ethanol (10% by volume) and ammonium oxalate (AO, 2 mM) were used as the scavengers of hydroxyl (·OH) and photogenerated holes (h^+), respectively [56]. N_2 purging can expel the dissolved O_2 in the solution, leading to the inhibition of superoxide ($\cdot O_2^-$) generation.

Photocatalytic Reduction of Cr(VI)

Cr(VI) was employed as another model pollutants to measure photocatalytic activity of the samples. The photocatalytic reduction process of Cr(VI) to Cr(III) was similar to that of the dye degradation. The initial concentration of Cr(VI) was 10 mg/l and the photocatalyst dosage was 0.2 g in 200 ml Cr(VI) solution (i.e., 1 g/l). The initial pH value of the Cr(VI) solution was adjusted by H_2SO_4 to 2~3. The residual concentration of Cr(VI) solution was detected by UV-vis spectrophotometer using the diphenylcarbazide (DPC) method [57].

Hydroxyl Radical Detections

Fluorimetry was employed to detect the ·OH radicals generated on the irradiated samples by using terephthalic acid (TA) as a probe molecule. Generally, the ·OH will react with TA to generate highly fluorescent compound, 2-hydroxyterephthalic acid (TAOH). The information of ·OH can be detected through measuring the photoluminescence (PL) intensity of TAOH with the excitation wavelength of ~ 315 nm. Typically, the TA was introduced into NaOH solution (1.0 mmol l^{-1}) to obtain TA solution (0.25 mmol l^{-1}). The catalyst (60 mg) was placed into TA solution (100 ml) under magnetically stirring for several minutes. After that, a certain amount of H_2O_2 was dissolved into above mixture, which was irradiated by visible light (300-W xenon lamp with a 420-nm cutoff filter) or NIR light (300-W xenon lamp with a 800-nm cutoff filter). At given intervals of irradiation, 3 ml of the reaction solution was sampled and centrifuged to remove the catalyst. The PL spectra of the supernatant were determined by fluorescence spectrophotometer. On the other hand, the generation of ·OH in the photocatalytic reaction was also measured under the same conditions without the addition of H_2O_2.

Characterization

The phase purity of the samples was examined by X-ray powder diffraction (XRD) and Fourier-transform infrared spectroscopy (FTIR). The morphology and microstructure of the samples were observed by field-emission transmission electron microscopy (TEM). The chemical states of the surface elements on the samples were detected by X-ray photoelectron spectroscopy (XPS). The ultraviolet-visible (UV-vis) diffuse reflectance spectra of the samples were recorded through a TU-1901 double beam UV-vis spectrophotometer. The PL spectra of the samples were determined by a fluorescence spectrophotometer. The transient photocurrent response and electrochemical impedance spectroscopy (EIS) measurements were carried out on an electrochemical workstation with a three-electrode system. The working electrode fabrication and test procedures were similar to those previously reported [56]. Particularly, the photocurrent response measurement was performed under visible light (300-W xenon lamp with a 420-nm cutoff filter) irradiation.

Results and Discussion

XRD Analysis

Figure 2 presents the XRD patterns of $BiFeO_3$, CQDs, and 24C/BFO. The $BiFeO_3$ and 24C/BFO sample show similar diffraction patterns, which can be readily indexed to the rhombohedral $BiFeO_3$ phase (JCPD file no: 74-2016). No trace of impurities, such as Fe_2O_3 and Bi_2O_3, is found. The results indicate that the high-purity $BiFeO_3$ is obtained and the introduction of CQDs and hydrothermal treatment do not obviously change the crystal structure of $BiFeO_3$. From the XRD pattern of CQDs, one can see that a broad diffraction peak is observed at ~ 23.5°, which is mainly attributed to the amorphous structure of CQDs. Notably, for the composite, no characteristic diffraction peaks of CQDs are detected owing to the low content of CQDs in the 24C/BFO sample. To confirm the existence of CQDs in the composite, the FTIR characterization is performed.

FTIR Analysis

Figure 3 shows the FTIR spectra of $BiFeO_3$, CQD, and 12C/BFO composites. In the case of bare $BiFeO_3$, the peaks at ~ 440 cm^{-1} and ~ 560 cm^{-1} are assigned to the stretching and bending vibrations of Fe–O, which is consistent with the reported result [55]. For the CQDs, the deformation vibration for C–H at ~ 638 cm^{-1}, the stretching vibration for C–C at ~ 1630 cm^{-1}, and C–OH stretching at ~ 1120 cm^{-1} are found [58]. In addition, the characteristic peaks of $BiFeO_3$ and CQDs are detected in the spectrum of 12C/BFO composite. The results suggest the existence of CQDs and $BiFeO_3$ in the composite. Moreover, the peak located at ~ 1380 cm^{-1} is attributed to the stretching vibration of O–H from the absorbed H_2O [59].

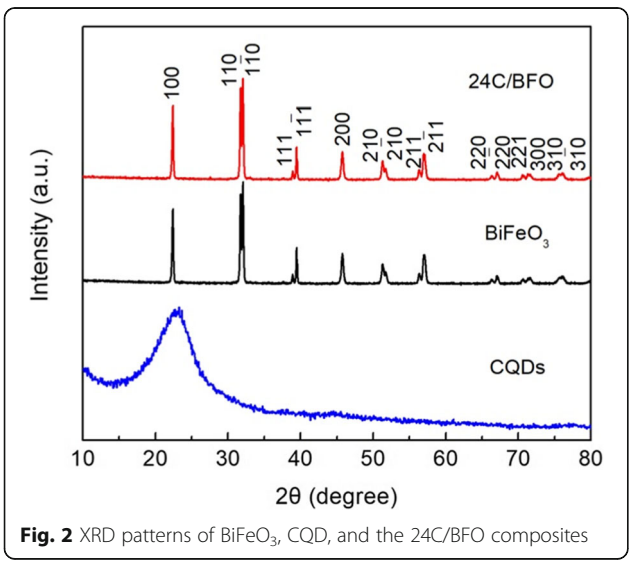

Fig. 2 XRD patterns of $BiFeO_3$, CQD, and the 24C/BFO composites

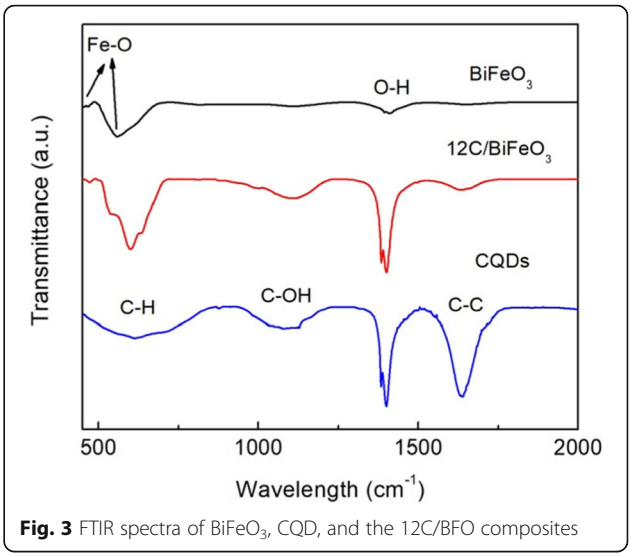

Fig. 3 FTIR spectra of $BiFeO_3$, CQD, and the 12C/BFO composites

Optical Absorption Property

It is well established that the optical absorption property of nanomaterials has an important effect on their performance [60, 61]. The optical absorption property of $BiFeO_3$, CQD, and CQDs/$BiFeO_3$ composites were investigated by UV-vis diffuse reflectance spectra, as shown in Fig. 4a. Compared with $BiFeO_3$, the CQD/$BiFeO_3$ composites exhibit obviously enhanced optical absorption capability in the entire UV-vis light region. It is worth noting that the optical absorption intensity of the composites gradually increases with increasing the content of CQDs. This phenomenon can be attributed to the strong light absorption of CQDs in the UV-vis light region. To obtain the light absorption edge of the samples, the first derivative curves of the UV-vis diffuse reflectance spectra are carried out (Fig. 4b), in which the peak wavelength is considered to be the absorption edge of the samples [62]. It is found that absorption edges of $BiFeO_3$ and CQD/$BiFeO_3$ composites are located at ~ 588 nm, suggesting that the decoration of CQDs does not change the bandgap energy of $BiFeO_3$.

XPS Analysis

The chemical states of elements in the 12C/BFO sample were monitored by XPS and the results are presented in Fig. 5. On the Bi 4f XPS spectrum (Fig. 5a), the observed two strong peaks at 164.1 (Bi $4f_{5/2}$) and 158.8 eV (Bi $4f_{7/2}$) demonstrate the existence of Bi^{3+} in the composite [63]. In Fig. 5b, the Fe 2p XPS spectrum indicates two obvious peaks at 723.6 and 709.6 eV, which are attributed to Fe $2p_{1/2}$ and Fe $2p_{3/2}$. Notably, the broad peak of Fe $2p_{3/2}$ can be divided into two peaks at 712.0 and 709.6 eV, corresponding to Fe^{3+} and Fe^{2+}, respectively [40]. In addition, it is seen that the satellite peak of Fe $2p_{3/2}$ is found at 717.8 eV. As shown in the XPS

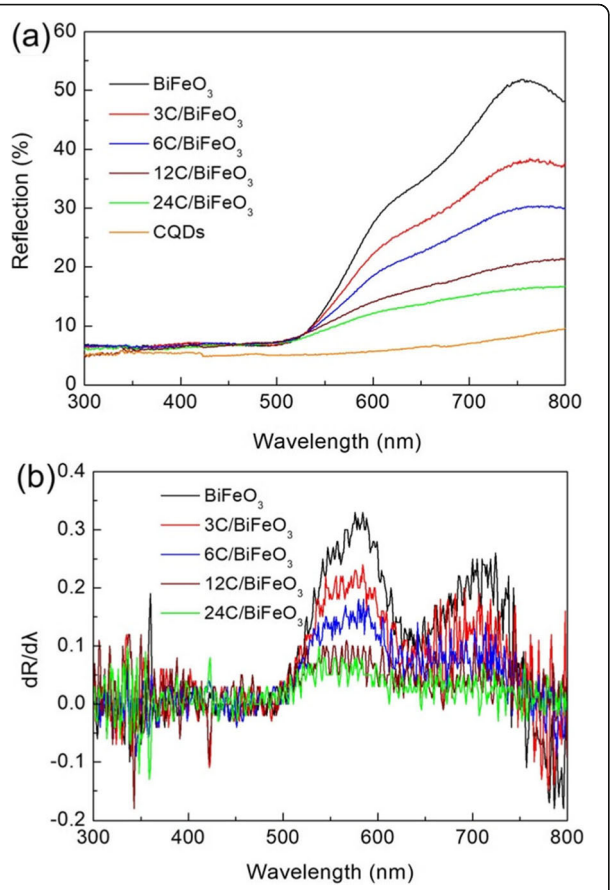

Fig. 4 **a** UV-vis diffuse reflectance spectra of $BiFeO_3$, CQD, and CQDs/$BiFeO_3$ composites. **b** The corresponding first derivative of the diffuse reflectance spectra

spectrum of O 1s (Fig. 5c), the obvious peak located at 529.6 eV is attributed to the lattice oxygen and the shoulder peak at 531.3 eV belongs to the chemisorbed oxygen of surface vacancies [64]. For the XPS spectrum of C 1s (Fig. 5d), the signal of C 1s can be divided into two distinct peaks. The major peak at ~ 284.9 eV is ascribed to the C–C bond with sp^2 orbital, whereas the peak at 287.7 eV is caused by the oxygenated carbon. The results further demonstrate the coexistence of CQDs and $BiFeO_3$ in the composite [65].

Morphology Observation

The TEM and high-resolution TEM (HRTEM) images of $BiFeO_3$ nanoparticles are shown in Fig. 6a and b, respectively. It is seen that the bare $BiFeO_3$ possesses a sphere-like shape and smooth surface with an average diameter of ~ 120 nm. The lattice spacing of 0.288 nm belongs to the (110) spacing of $BiFeO_3$. The TEM image in Fig. 6c indicates that the CQDs are composed of spherical-like particles with an average particle size of ~ 15 nm. From the TEM image of the CQD/$BiFeO_3$ composites (Fig. 6d–g), one can see that the CQDs are decorated on the surface of $BiFeO_3$ nanoparticles. The HRTEM image of the 12C/$BiFeO_3$ sample (Fig. 6h) reveals the interplanar distance of 0.389 nm corresponding to the (012) plane of $BiFeO_3$. Alongside of $BiFeO_3$, the decorated CQDs exhibit amorphous characteristic. This result suggests the formation of hybrid composite structure between $BiFeO_3$ and CQDs.

The dark-field scanning TEM (DF-STEM) image and the corresponding elemental mappings of the 12C/BFO sample are shown in Fig. 7a–e, respectively. The results reveal that the sample presents not only uniform distribution of the Bi/Fe/O elements but also uniform distribution of the C element. This confirms that CQDs are uniformly assembled on the surface of $BiFeO_3$ nanoparticles.

Photo-Fenton Catalytic and Photocatalytic Performance

The photocatalytic performance of the samples was first assessed by the degradation of AO7 under visible light irradiation, and the result is shown in Fig. 8a. Prior to the photocatalytic reaction, the adsorption (in the dark) and blank (without catalyst) experiments were carried out. A small amount of AO7 (~ 5%) is degraded after 3-h irradiation without catalyst, indicating that the self-degradation of the dye can be neglected. In the photocatalytic reaction, the photodegradation ability of pure $BiFeO_3$ is weak and only ~ 33% of AO7 is observed to be decomposed after 3-h exposure. When $BiFeO_3$ nanoparticles are decorated by CQDs, the CQD/$BiFeO_3$ composites exhibit obviously enhanced photocatalytic activity. Moreover, it is found that the catalytic activities of the composites are highly related to the content of CQDs. Among these composites, the 12C/$BiFeO_3$ composite displays the optimal degradation percentage of ~ 73% after 3-h irradiation, which is 2.2 times higher than that of bare $BiFeO_3$. However, with further increase of the CQD content (e.g., 24C/BFO), excessive CQDs decorated on the surface of $BiFeO_3$ nanoparticles may shield $BiFeO_3$ from absorbing visible light, which leads to the decrease of the photocatalytic activity.

In this work, the photocatalytic ability of the samples for the reduction of Cr(VI) under visible light irradiation was also studied, as shown in Fig. 8b. The blank experiment indicates that the reduction of Cr(VI) after 3-h illumination in the absence of catalysts is negligible. It is seen that the CQD/$BiFeO_3$ composites possess much higher photocatalytic reduction ability than pure $BiFeO_3$. The reduction efficiency of Cr(VI) over the samples increases in the order: $BiFeO_3$ < 3C/BFO < 6C/BFO < 24C/BFO < 12C/BFO. The result demonstrates the visible light-driven photocatalytic reduction property of $BiFeO_3$, which can be obviously improved by the decoration of CQDs.

Besides the photocatalytic activity, it is demonstrated that $BiFeO_3$ also displays promising photo-Fenton-like

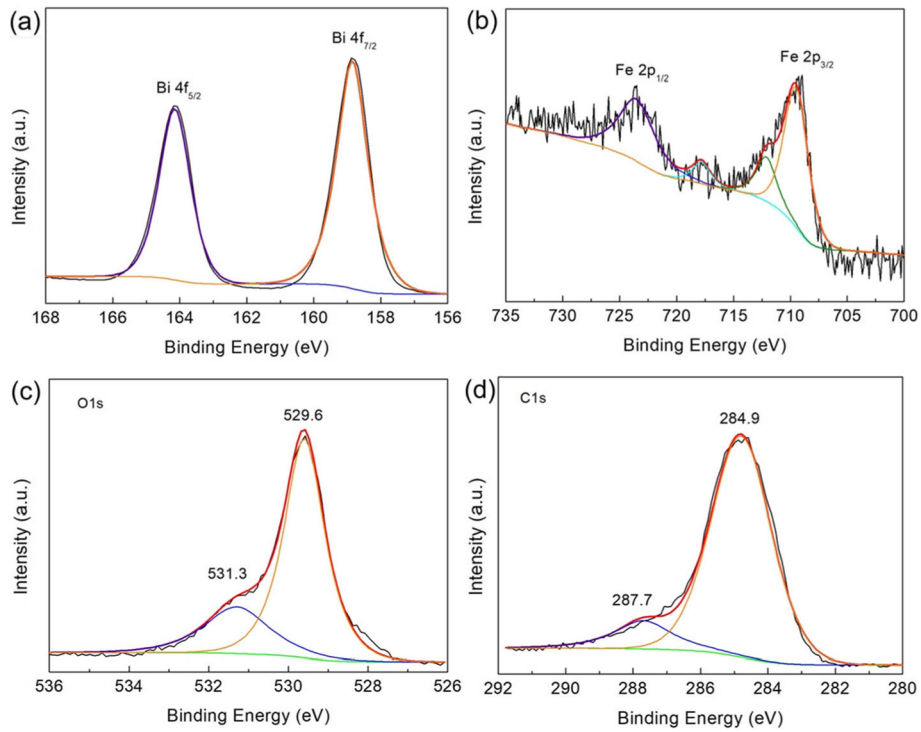

Fig. 5 High-resolution XPS spectra of **a** Bi 4f, **b** Fe 2p, **c** O 1s, and **d** C 1s for the 12C/BFO composite

catalysis ability. Figure 8c shows the photo-Fenton degradation of AO7 over the samples under visible light irradiation with the addition of H_2O_2, from which one can see that the degradation percentage of AO7 in the photo-Fenton-like catalytic process is much higher than that in bare photocatalytic reaction. For example, about 96% of AO7 is photo-Fenton catalytically degraded over 12C/BFO sample under 3-h irradiation, which has a ~ 23% enhancement compared with the photocatalytic degradation of AO7 (~ 73%). In addition, it is found that the photo-Fenton catalytic activities between the samples have an order same to the photocatalytic activities between the samples. This suggests that the CQD/$BiFeO_3$ composites can be used as effective photo-Fenton catalysts for the degradation of dyes.

Generally, the reusability of catalysts is regarded as an important parameter for their practical application. According to above catalytic results, the 12C/BFO sample was chosen as the catalyst for the investigation of photocatalytic and photo-Fenton catalytic stabilities. Figure 8d presents the catalytic activities of the 12C/BFO sample during three successive visible light-driven photocatalytic and photo-Fenton catalytic processes. After three consecutive cycles, the catalytic activities of the 12C/BFO sample do not undergo obvious decrease. This indicates that the CQD/$BiFeO_3$ composite exhibits good catalytic reusability under visible light irradiation.

In this work, the NIR light-driven photocatalytic and photo-Fenton catalytic activities of $BiFeO_3$ and 12C/BFO were investigated. Figure 9a–c display the time-dependent photocatalytic degradation of AO7, photocatalytic reduction of Cr(VI), and photo-Fenton catalytic degradation of AO7 over $BiFeO_3$ and 12C/$BiFeO_3$ under NIR light irradiation, respectively. It can be seen that bare $BiFeO_3$ exhibits almost no NIR light photocatalytic activity because it cannot respond to NIR light, while about 22% of AO7 is degraded by $BiFeO_3$ during the photo-Fenton catalytic reaction. In contrast, the 12C/BFO sample displays obvious NIR light-driven catalytic activities. After 3-h NIR light irradiation, the photocatalytic degradation of AO7, photocatalytic reduction of Cr(VI), and photo-Fenton degradation of AO7 over the 12C/BFO sample reach ~ 35%, ~ 63%, and ~ 49%, respectively. The result indicates that the introduction of CQDs onto the surface of $BiFeO_3$ plays an important role in the enhancement of its NIR light-driven catalytic activity. The NIR light catalytic stabilities of the 12C/BFO sample were also studied by recycling catalytic experiments, as shown in Fig. 9d. It is found that the CQD/$BiFeO_3$ composite also has steady NIR light-driven catalytic activity.

Active Species Trapping

To explore the effect of active species on the catalytic degradation reaction, reactive species trapping experiments

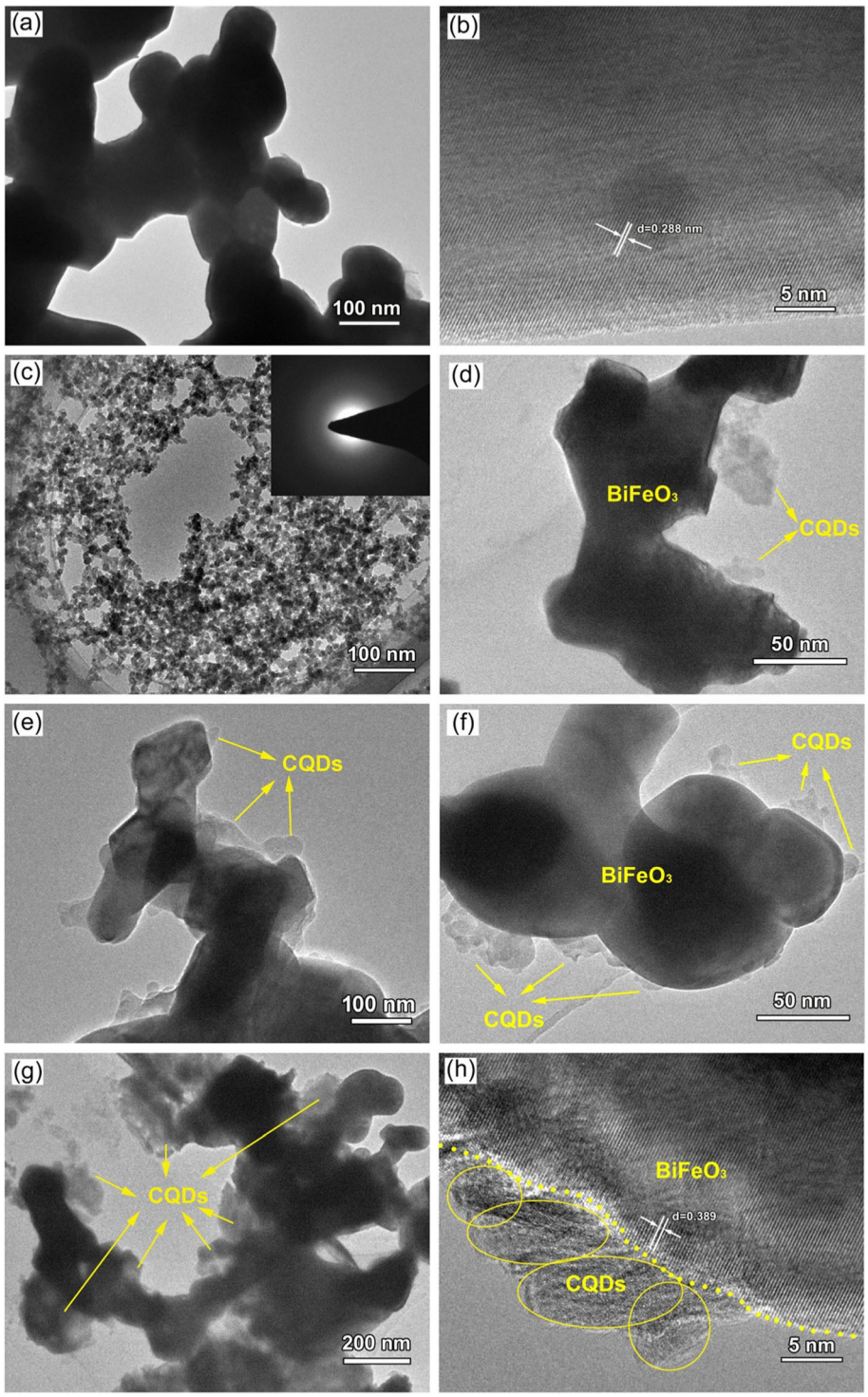

Fig. 6 **a** and **b** TEM and HRTEM images of bare $BiFeO_3$ nanoparticles, respectively; **c** TEM image of CQDs; **d**–**g** TEM images of 3C/BFO, 6C/BFO 12C/BFO, and 24C/BFO respectively; **h** HRTEM image of 12C/BFO

were carried out. Figure 10a and b show the photocatalytic and photo-Fenton catalytic degradation of AO7 using the 12C/BFO sample with the addition of quenchers under visible light illumination, respectively. From Fig. 10a, the introduction of ethanol and AO leads to relatively small inhibition on the AO7 degradation. In contrast, the photocatalytic degradation of AO7 is dramatically suppressed with N_2 purging. This suggests that the $\cdot O_2^-$ is the primary reactive

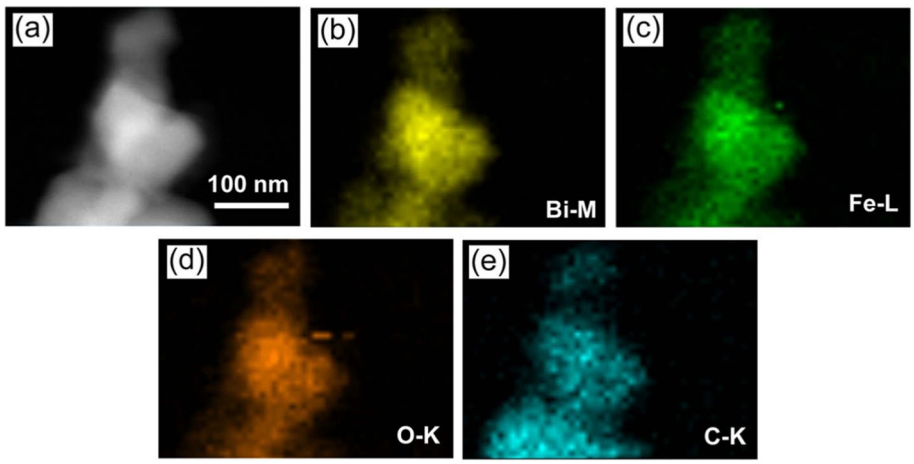

Fig. 7 a DF-STEM image of the 12C/BFO composite. **b**–**e** The corresponding energy dispersive X-ray elemental mapping images

species, whereas ·OH and h^+ are the secondary reactive species responsible for the dye degradation. As shown in Fig. 10b, the degradation percentage of AO7 decreases from 96% (without scavengers) separately to ~ 60% (N_2 purging), ~ 71% (adding AO), and ~ 45% (adding ethanol). This reveals that $\cdot O_2^-$, h^+, and ·OH participate in the visible light-driven photo-Fenton catalytic reaction, and ·OH plays a relatively large role in this process. Figure 10c and d present the photocatalytic and photo-Fenton catalytic degradation of AO7 over the 12C/BFO sample in the presence of scavengers with the irradiation of NIR light, respectively. It can be seen that in the both catalytic processes, the dye degradation depends on $\cdot O_2^-$, h^+, and ·OH. Particularly, $\cdot O_2^-$ is demonstrated to be the main active species in the NIR light-driven

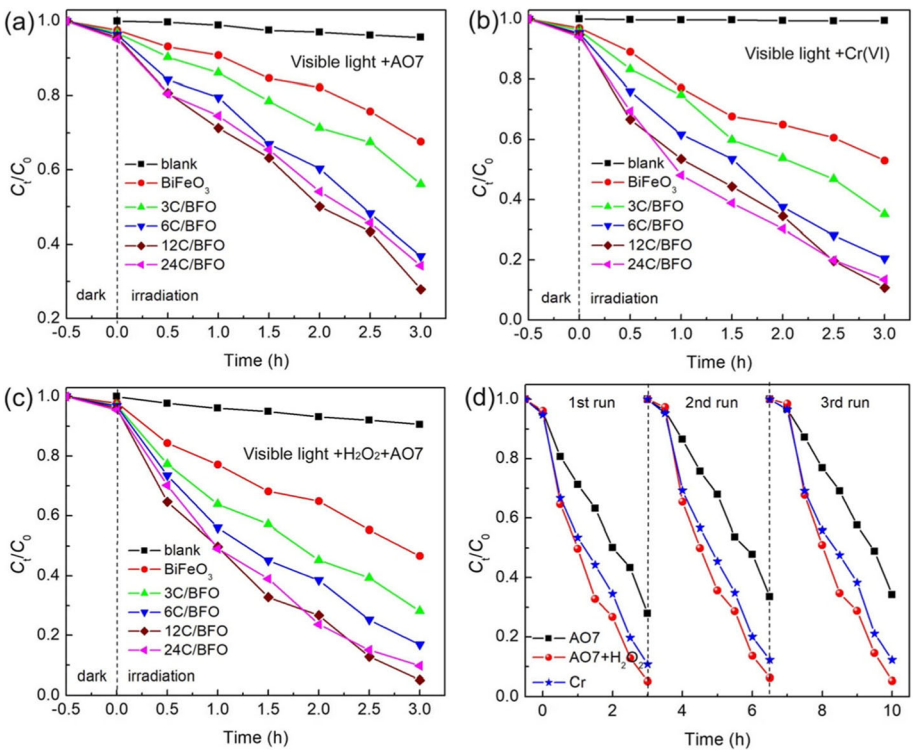

Fig. 8 a Photocatalytic degradation of AO7, **b** photocatalytic reduction of Cr(VI), and **c** photo-Fenton catalytic degradation of AO7 over $BiFeO_3$ and CQD/$BiFeO_3$ composites under visible light irradiation. **d** Recyclability of the 12C/BFO composite for photocatalytic degradation of AO7, photocatalytic reduction of Cr(VI), and photo-Fenton catalytic degradation of AO7 under visible light irradiation

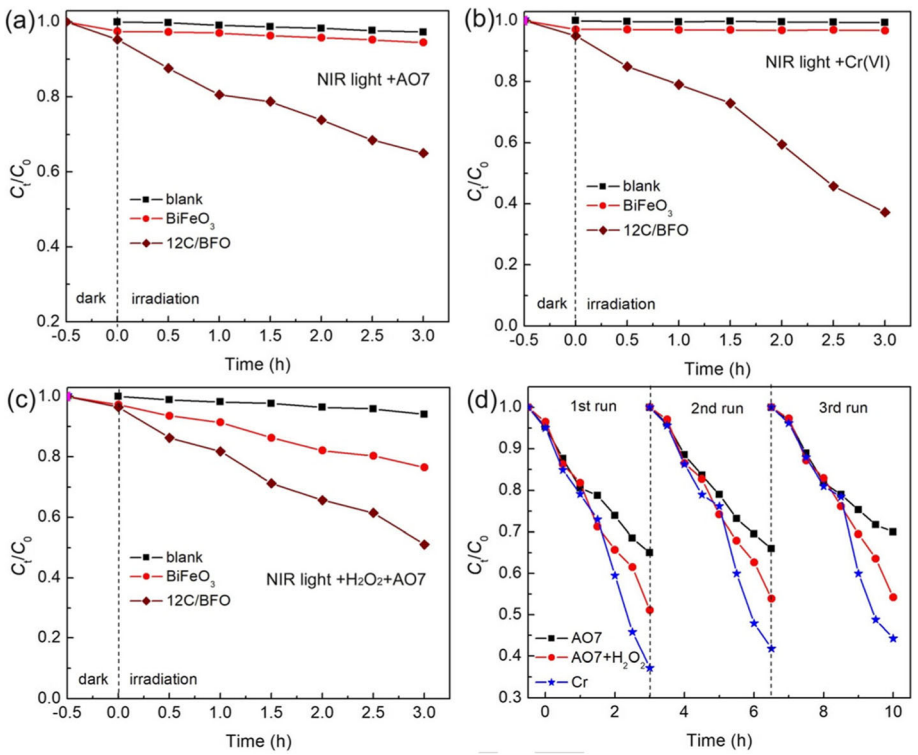

Fig. 9 **a** Photocatalytic degradation of AO7, **b** photocatalytic reduction of Cr(VI), and **c** photo-Fenton catalytic degradation of AO7 over $BiFeO_3$ and CQD/$BiFeO_3$ composites under NIR light irradiation. **d** Recyclability of the 12C/BFO composite for photocatalytic degradation of AO7, photocatalytic reduction of Cr(VI), and photo-Fenton catalytic degradation of AO7 under NIR light irradiation

photocatalytic process, whereas ·OH exhibits a key duty in the NIR light photo-Fenton catalytic reaction.

Figure 11 displays the time-dependent PL spectra of the TPA solution using the 12C/BFO sample as the catalyst in the photocatalytic and photo-Fenton catalytic reaction under visible and NIR light illumination. It is seen that, in all cases of the catalytic processes, the PL emission peak located at ~ 429 nm becomes intense gradually with the increase of the illumination time, indicating the generation of ·OH radicals. Based on the PL signal intensity, it is concluded that more ·OH radicals are generated in the photo-Fenton process than in the photocatalytic process, and the visible light irradiation leads to the increased generation of ·OH radicals when compared with the NIR light irradiation.

Photogenerated Charges Performance

Photoelectrochemical measurement is very useful for the investigation of the migration and recombination performance of photogenerated charges. The transient photoresponse currents of $BiFeO_3$ and 12C/BFO under visible light irradiation with several on/off cycles are shown in Fig. 12a. One can see that the photocurrent density of 12C/BFO is much higher than that of bare $BiFeO_3$, indicating the effective separation of photogenerated charges in the CQDs/$BiFeO_3$ composite. Figure 12b displays the EIS curves of $BiFeO_3$ and 12C/BFO. It is well known that the semicircle in the Nyquist plot at the high-frequency region reflects the interfacial charge-transfer process and a smaller diameter of semicircle means a lower charge-transfer resistance [66]. The 12C/BFO sample exhibits a smaller semicircle diameter compared with bare $BiFeO_3$, suggesting that the migration of photogenerated charges can be promoted in the CQD/$BiFeO_3$ composites.

Catalytic Mechanism

A possible visible light-driven photocatalytic mechanism of CQDs/$BiFeO_3$ for the dye degradation and Cr(VI) reduction is proposed, as shown in Fig. 13a. When the CQD/$BiFeO_3$ composite is irradiated by visible light, the $BiFeO_3$ nanoparticles will be excited to generate photogenerated electrons and holes. On the other hand, the electrons in the CQDs can be also excited from their π orbital or σ orbital to the lowest unoccupied molecular orbital (LUMO) to obtain photoexcited electrons. It has been demonstrated that the excited CQDs can act as excellent electron donors and electron acceptors.

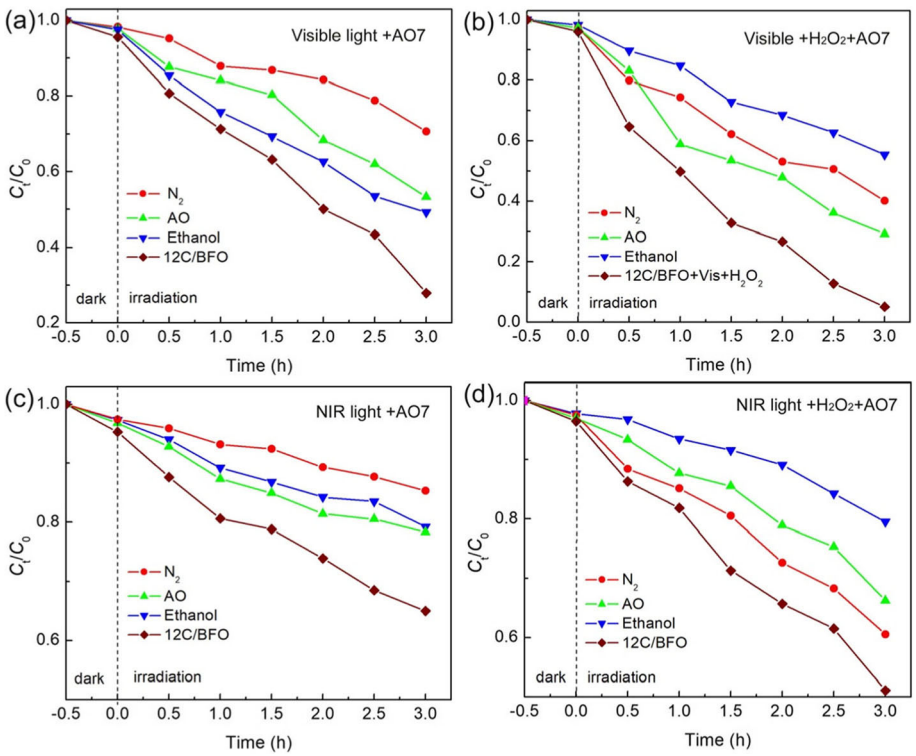

Fig. 10 **a** and **b** Effects of ethanol, N_2 purging, and AO on the photocatalytic and photo-Fenton catalytic degradation of AO7 over 12C/BFO under visible light irradiation, respectively. **c** and **d** Effects of ethanol, N_2 purging, and AO on the photocatalytic and photo-Fenton catalytic degradation of AO7 over 12C/BFO under NIR light irradiation, respectively

Therefore, the photogenerated electrons in the conduction band (CB) of $BiFeO_3$ nanoparticles will easily migrate to the π orbital or σ orbital of CQDs, while the photoexcited electrons of CQDs will transfer to the CB of $BiFeO_3$. During the above converse electron migration process, the separation of photogenerated charges in $BiFeO_3$ can be promoted, as revealed by photoelectrochemical measurement (see Fig. 12a). Thus, more photogenerated charges are available for participating in the photocatalytic reaction, leading to the improvement of photocatalytic activity.

More importantly, the up-converted PL property of CQDs also plays an important role in the enhancement of photocatalytic activity. Figure 13b presents the up-converted PL spectra of CQDs with the excitation wavelength from 810 to 890 nm, from which one can see that the up-converted emission peaks are centered at shorter wavelengths in the range of 400–680 nm. Because the light absorption edge of the as-prepared $BiFeO_3$ nanoparticles is located at ~ 588 nm (see Fig. 4), the up-converted emission light (400–588 nm) of CQDs can be used to excite $BiFeO_3$ nanoparticles to produce photogenerated electrons and holes, which provides additional photogenerated charges for the photocatalytic reaction. This also contributes to the enhancement of photocatalytic activity for $BiFeO_3$ nanoparticles.

Besides the yield of photogenerated charges, the redox ability of photogenerated charges is considered to be another important factor for understanding the catalytic mechanism of catalysts. In our previous work, the CB and VB potentials of prepared $BiFeO_3$ nanoparticles are calculated to be + 0.4 and + 2.47 V vs. NHE, respectively [55]. From a thermodynamic point of view, the generation of ·OH will be smoothly achieved because the VB potential of $BiFeO_3$ is more positive than the redox potential of $OH^-/{\cdot}OH$ (+ 1.99 V vs. NHE) [67]. Compared with the redox potential of Cr(VI)/Cr(III) (+ 0.51 V vs. NHE) [57], the photogenerated electrons in the CB of $BiFeO_3$ is negative enough to reduce Cr(VI) to Cr(III). Another active species $\cdot O_2^-$ can be obtained from the reaction between the photoexcited electrons of CQDs and O_2 [68].

Figure 13c presents the visible light-driven photo-Fenton catalytic degradation mechanism of the dye over the CQD/$BiFeO_3$ composites. In this case, the photocatalytic and Fenton reactions will simultaneously happen. When H_2O_2 is introduced into visible light-driven photocatalytic system, the H_2O_2 can react with Fe^{2+} on

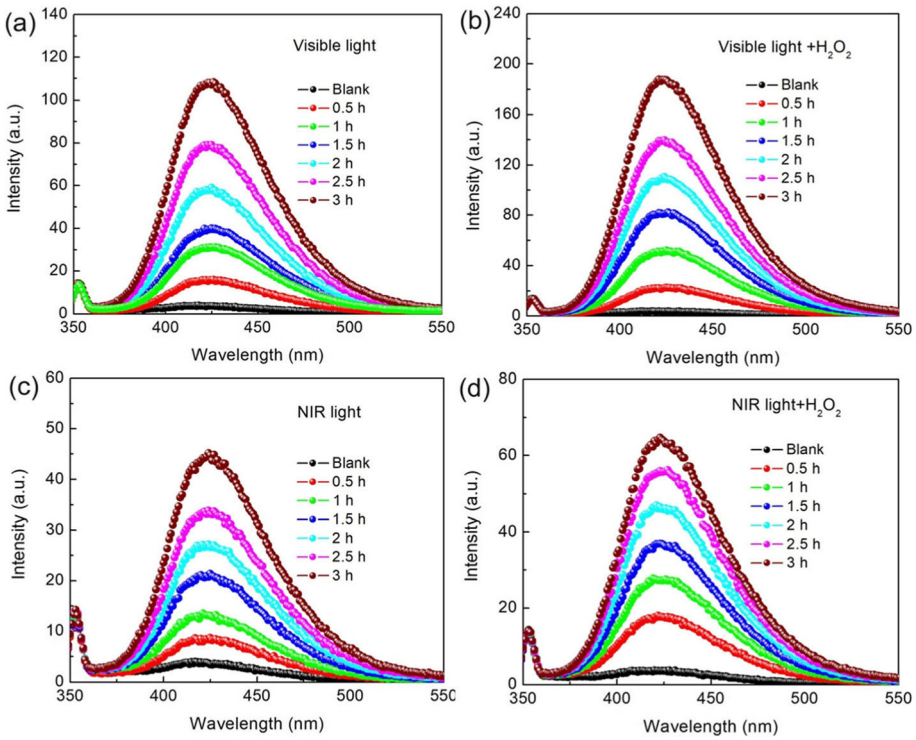

Fig. 11 **a** and **b** PL spectra of the TA solution as a function of visible light irradiation time over the 12C/BFO sample in the photocatalytic and photo-Fenton catalytic reactions, respectively. **c** and **d** PL spectra of the TA solution as a function of NIR light irradiation time over the 12C/BFO sample in the photocatalytic and photo-Fenton catalytic reactions, respectively

the surface of $BiFeO_3$ to obtain additional ·OH along with the generation of Fe^{3+}. Simultaneously, the Fe^{3+} will be reduced to Fe^{2+} by the photogenerated electrons of $BiFeO_3$ and CQDs [69]. During this cycle reaction, more ·OH is produced, which is beneficial for the enhancement of catalytic efficiency.

Figure 13d and e display the photocatalytic and photo-Fenton catalytic mechanism of the CQDs/$BiFeO_3$ composite under NIR light irradiation. It is known that the $BiFeO_3$ do not response to NIR light (> 800 nm). As a result, only CQDs can be excited under NIR light irradiation in the two catalytic processes. The photogenerated charges migration and up-converted excitation of CQDs are similar to those as depicted in Fig. 13a and b. Because the $BiFeO_3$ cannot be directly excited by NIR light, NIR light-excited CQD/$BiFeO_3$ composite has a relatively lower yield of photogenerated charges compared with the visible light-excited composite. This is why photocatalytic and photo-Fenton catalytic activities of the CQD/$BiFeO_3$ composites under NIR light irradiation are weaker than those under visible light irradiation.

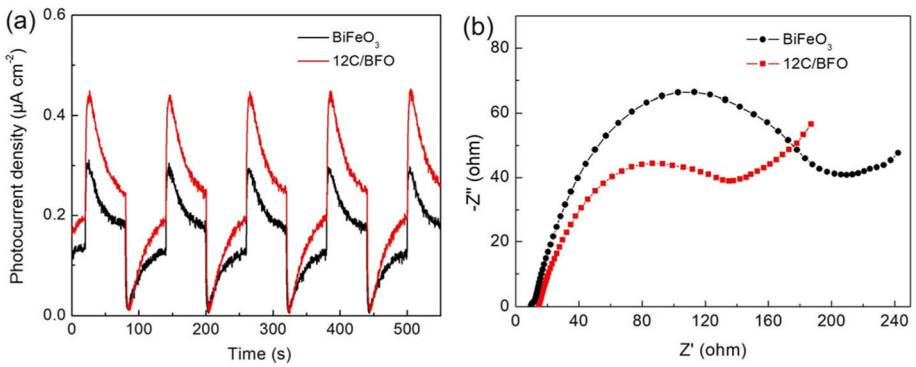

Fig. 12 **a** Photocurrent response plots of $BiFeO_3$ and 12C/BFO under visible light irradiation. **b** EIS spectra of $BiFeO_3$ and 12C/BFO

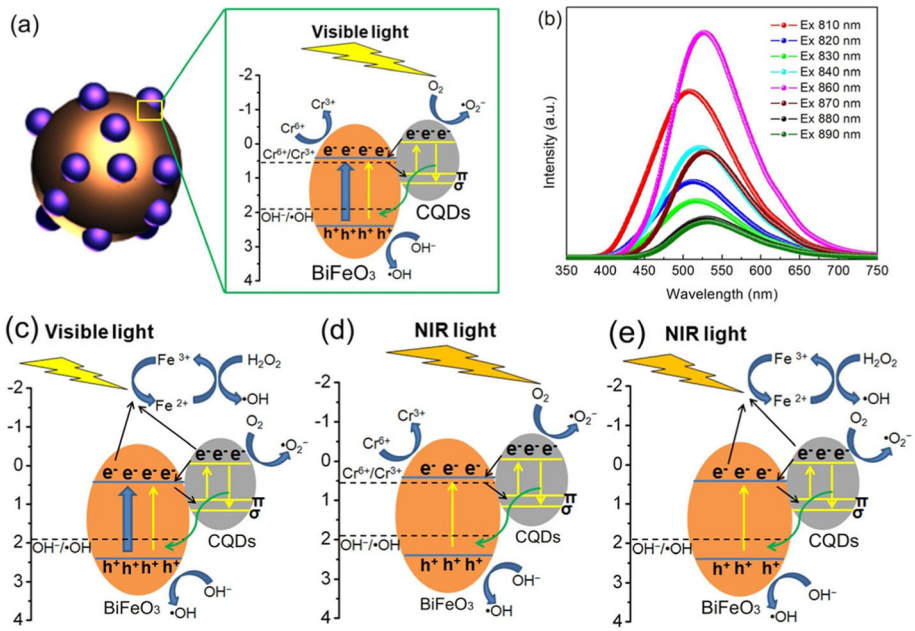

Fig. 13 a Photocatalytic degradation mechanism of AO7 over the CQDs/$BiFeO_3$ composite photocatalysts under visible light irradiation. **b** Up-converted PL spectra of CQDs under different excitation wavelengths. **c** Photo-Fenton catalytic degradation mechanism of AO7 over the CQD/$BiFeO_3$ composites under visible light irradiation. **d** NIR light photocatalytic mechanism of the CQDs/$BiFeO_3$ composites. **e** NIR light photo-Fenton mechanism of the CQD/$BiFeO_3$ composites

Conclusions

The CQDs were successfully decorated on the surface of $BiFeO_3$ nanoparticles through a hydrothermal route to obtain CQD/$BiFeO_3$ composites. Under visible and NIR light irradiation, these composites manifest remarkably enhanced photocatalytic degradation of AO7, photocatalytic reduction of Cr(VI), and photo-Fenton catalytic degradation of AO7 compared with bare $BiFeO_3$ nanoparticles. They can be reused without obvious decrease of catalytic activities. It is found that the introduction of CQDs leads to the efficient separation of photogenerated charges in the composites. The improved catalytic activities of CQD/$BiFeO_3$ composites can be ascribed to the two factors: the excellent up-converted photoluminescence property and photogenerated electron transfer ability of CQDs.

Abbreviations

AO: Ammonium oxalate; AO7: Acid orange 7; CB: Conduction band; CQDs: Carbon quantum dots; Cr(VI): Hexavalent chromium; DF-STEM: Dark-field scanning transmission electron microscope; DPC: Diphenylcarbazide method; DRS: UV-vis diffuse reflectance spectra; E_g: Bandgap energy; EIS: Electrochemical impedance spectroscopy; FTIR: Fourier-transform infrared spectroscopy; h^+: Photogenerated holes; HRTEM: High-resolution transmission electron microscope; LUMO: Lowest unoccupied molecular orbital; NIR: Near-infrared light; O_2^-: Superoxide radical; OH: Hydroxyl radical; PL: Photoluminescence; TA: Terephthalic acid; TAOH: 2-Hydroxyterephthalic acid; TEM: Transmission electron microscope; VB: Valence band; XPS: X-ray photoelectron spectroscopy; XRD: X-ray diffractometer

Acknowledgements

The authors appreciate the National Natural Science Foundation of China (Grant No. 51602170), the Natural Science Foundation of Qinghai, China (Grant No.2016-ZJ-954Q), and the Youth Science Foundation of Qinghai Normal University (Grant No. 2019zr003).

Authors' contributions

TX and LD conceived the idea of experiments. LD, XS, HL and YZ performed the experiments. TX and LD discussed and analyzed the experimental results. TX and LD drafted the manuscript. HY revised the manuscript. All authors read and approved the final manuscript.

Funding

This work was supported by the National Natural Science Foundation of China (Grant No. 51602170), the Natural Science Foundation of Qinghai, China (Grant No.2016-ZJ-954Q), and the Youth Science Foundation of Qinghai Normal University (Grant No. 2019zr003).

Availability of data and materials

All data analyzed during this investigation are presented in this article.

Competing interests

The authors declare that they have no competing interests and the mentioned received funding in our manuscript does not lead to any conflict of interests regarding the publication of this work.

Author details

[1]College of Physics and Electronic Information Engineering, Qinghai Normal University, Xining 810008, China. [2]State Key Laboratory of Advanced Processing and Recycling of Non-Ferrous Metals, Lanzhou University of Technology, Lanzhou 730050, China.

Received: 29 August 2019 Accepted: 8 November 2019
Published online: 30 December 2019

References

1. Richard FC, Bourg A (1991) Aqueous geochemistry of chromium: a review. Water Res 25:807–816
2. Brown MA, De Vito SC (1993) Predicting azo dye toxicity. Crit Rev Environ Sci Technol 23:249–324

3. Li H, Li Z, Liu T, Xiao X, Peng Z, Deng L (2008) A novel technology for biosorption and recovery hexavalent chromium in wastewater by bio-functional magnetic beads. Bioresour Techno 99:6271–6279
4. Teh CY, Budiman PM, Shak KPY, Wu TY (2016) Recent advancement of coagulation-flocculation and its application in wastewater treatment. Ind Eng Chem Res 55:4363–4389
5. Yi Z, Li X, Wu H, Chen XF, Yang H, Tang YJ, Yi YG, Wang JQ, Wu PH (2019) Fabrication of ZnO@Ag_3PO_4 core-shell nanocomposite arrays as photoanodes and their photoelectric properties. Nanomaterials 9:1254
6. Wang SY, Yang H, Yi Z, Wang XX (2019) Enhanced photocatalytic performance by hybridization of Bi_2WO_6 nanoparticles with honeycomb-like porous carbon skeleton. J Environ Manage 248:109341
7. Yan YX, Yang H, Yi Z, Xian T (2019) $NaBH_4$-reduction induced evolution of Bi nanoparticles from BiOCl nanoplates and construction of promising Bi@BiOCl hybrid photocatalysts. Catalysts 9:795
8. Li MR, Song C, Wu Y, Wang M, Pan ZP, Sun Y, Meng L, Han SG, Xu LJ, Gan L (2019) Novel Z-scheme visible-light photocatalyst based on $CoFe_2O_4$/BiOBr/Graphene composites for organic dye degradation and Cr(VI) reduction. Appl Surf Sci 478:744–753
9. Palas B, Ersöz G, Atalay S (2017) Photo Fenton-like oxidation of tartrazine under visible and UV light irradiation in the presence of $LaCuO_3$ perovskite catalyst. Process Saf Environ Prot 111:270–282
10. Yamashita H, Mori K, Kuwahara Y, Kamegawa T, Wen MC, Verma P, Che M (2018) Single-site and nano-confined photocatalysts designed in porous materials for environmental uses and solar fuels. Chem Soc Rev 47:8072–8096
11. Fujishima A, Zhang X, Tryk DA (2007) Heterogeneous photocatalysis: from water photolysis to applications in environmental cleanup. Int J Hydrogen Energy 32:2664–2672
12. Shiraz AD, Takdastan A, Borghei SM (2018) Photo-Fenton like degradation of catechol using persulfate activated by UV and ferrous ions: influencing operational parameters and feasibility studies. J Mol Liq 249:463–369
13. Valero-Luna C, Palomares-Sanchez SA, Ruiz F (2016) Catalytic activity of the barium hexaferrite with H_2O_2/visible light irradiation for degradation of methylene blue. Catal Today 266:110–119
14. Yi Z, Zeng Y, Wu H, Chen XF, Fan YX, Yang H, Tang YJ, Yi YG, Wang JQ, Wu PH (2019) Synthesis, surface properties, crystal structure and dye-sensitized solar cell performance of TiO_2 nanotube arrays anodized under different parameters. Results Phys 15:102609
15. Yu PQ, Chen XF, Yi Z, Tang YJ, Yang H, Zhou ZG, Duan T, Cheng SB, Zhang JG, Yi YG (2019) A numerical research of wideband solar absorber based on refractory metal from visible to near infrared. Opt Mater 97:109400
16. Liang CP, Yi Z, Chen XF, Tang YJ, Yi Y, Zhou ZG, Wu XG, Huang Z, Yi YG, Zhang GF (2019) Dual-band infrared perfect absorber based on a Ag-dielectric-Ag multilayer films with nanoring grooves arrays. Plasmonics. https://doi.org/10.1007/s11468-019-01018-4
17. Tian J, Leng YH, Zhao ZH, Xia Y, Sang YH, Hao P, Zhan J, Li MC, Liu H (2015) Carbon quantum dots/hydrogenated TiO_2 nanobelt heterostructures and their broad spectrum photocatalytic properties under UV, visible, and near-infrared irradiation. Nano Energy 11:419–427
18. Wei N, Cui HZ, Song Q, Zhang LQ, Song XJ, Wang K, Zhang YF, Li J, Wen J, Tian J (2016) Ag_2O nanoparticle/TiO_2 nanobelt heterostructures with remarkable photo-response and photocatalytic properties under UV, visible and near-infrared irradiation. Appl Catal B Environ 198:83–90
19. Hu XL, Li YY, Tian J, Yang HR, Cui HZ (2017) Highly efficient full solar spectrum (UV-vis-NIR) photocatalytic performance of Ag_2S quantum dot/TiO_2 nanobelt heterostructures. J Ind Eng Chem 45:189–196
20. Di LJ, Xian T, Sun XF, Li HQ, Zhou YJ, Ma J, Yang H (2019) Facile preparation of CNT/Ag_2S nanocomposites with improved visible and NIR light photocatalytic degradation activity and their catalytic mechanism. Micromachines 10:503
21. Yu L, Chen JD, Liang Z, Xu WC, Chen LM, Ye DQ (2016) Degradation of phenol using Fe_3O_4-GO nanocomposite as a heterogeneous photo-Fenton catalyst. Sep Purif Technol 171:80–87
22. Guo XJ, Wang KB, Li D, Qin JB (2017) Heterogeneous photo-Fenton processes using graphite carbon coating hollow $CuFe_2O_4$ spheres for the degradation of methylene blue. Appl Surf Sci 420:792–801
23. Di LJ, Yang H, Xian T, Liu XQ, Chen XJ (2019) Photocatalytic and photo-Fenton catalytic degradation activities of Z-scheme Ag_2S/$BiFeO_3$ heterojunction composites under visible-light irradiation. Nanomaterials 9:399
24. Cai C, Zhang ZY, Liu J, Shan N, Zhang H, Dionysiou DD (2016) Visible light-assisted heterogeneous Fenton with $ZnFe_2O_4$ for the degradation of Orange II in water. Appl Catal B Environ 182:456–468
25. Liang C, Liu YH, Li K, Wen J, Xing ST, Ma ZC, Wu YS (2017) Heterogeneous photo-Fenton degradation of organic pollutants with amorphous Fe-Zn-oxide/hydrochar under visible light irradiation. Sep Purif Technol 188:105–111
26. Gao F, Chen XY, Yin KB, Dong S, Ren ZF, Yuan F, Yu T, Zou ZG, Liu JM (2007) Visible-light photocatalytic properties of weak magnetic $BiFeO_3$ nanoparticles. Adv Mater 19:2889–2892
27. Rabbani M, Rahimi R, Ghadi HF (2018) Photocatalytic application of $BiFeO_3$ synthesized via a facile microwave-assisted solution combustion method. J Sol-Gel Sci Technol 87:340–346
28. Basith MA, Yesmin N, Hossain R (2018) Low temperature synthesis of $BiFeO_3$ nanoparticles with enhanced magnetization and promising photocatalytic performance in dye degradation and hydrogen evolution. RSC Adv 8:29613–29627
29. Lam SM, Sin JC, Mohamed AR (2017) A newly emerging visible light-responsive $BiFeO_3$ perovskite for photocatalytic applications: a mini review. Mater Res Bull 90:15–30
30. Bai XF, Wei J, Tian BB, Liu Y, Reiss T, Guiblin N, Gemeiner P, Dkhil B, Infante IC (2016) Size effect on optical and photocatalytic properties in $BiFeO_3$ nanoparticles. J Phys Chem C 120:3595–3601
31. Ji W, Yao K, Lim YF, Liang YC, Suwardi A (2013) Epitaxial ferroelectric $BiFeO_3$ thin films for unassisted photocatalytic water splitting. Appl Phys Lett 103:062901
32. Bharathkumar S, Sakar M, Vinod RK, Balakumar S (2015) Versatility of electrospinning in the fabrication of fibrous mat and mesh nanostructures of bismuth ferrite ($BiFeO_3$) and their magnetic and photocatalytic activities. Phys Chem Chem. Phys 17:17745–17754
33. Jia YF, Wu CJ, Kim DH, Lee BW, Rhee SJ, Park YC, Kim CS, Wang QJ, Liu CL (2018) Nitrogen doped $BiFeO_3$ with enhanced magnetic properties and photo-Fenton catalytic activity for degradation of bisphenol A under visible light. Chem Eng J 337:709–721
34. Soltani T, Lee BK (2017) Enhanced formation of sulfate radicals by metal-doped $BiFeO_3$ under visible light for improving photo-Fenton catalytic degradation of 2-chlorophenol. Chem Eng J 313:1258–1268
35. Vanga PR, Mangalaraja RV, Ashok M (2016) Effect of co-doping on the optical, magnetic and photocatalytic properties of the Gd modified $BiFeO_3$. J Mater Sci -Mater Electron 27:5699–5706
36. Tovstolytkin NA, Lotey GS (2017) Plasmonic enhanced photocatalytic activity of Ag nanospheres decorated $BiFeO_3$ nanoparticles. Catal Lett 147:1640–1645
37. Tang JH, Wang RX, Liu MY, Zhang ZH, Song YT, Xue S, Zhao ZG, Dionysiou DD (2018) Construction of novel Z-scheme Ag/$FeTiO_3$/Ag/$BiFeO_3$ photocatalyst with enhanced visible-light-driven photocatalytic performance for degradation of norfloxacin. Chem Eng J 351:1056–1066
38. Li HF, Quan X, Chen S, Yu HT (2017) Ferroelectric-enhanced Z-schematic electron transfer in $BiVO_4$-$BiFeO_3$-$CuInS_2$ for efficient photocatalytic pollutant degradation. Appl Catal B Environ 209:591–599
39. Wang XF, Mao WW, Zhang J, Han YM, Quan CY, Zhang QX, Yang T, Yang JP, Li XA, Huang W (2015) Facile fabrication of highly efficient g-C_3N_4/$BiFeO_3$ nanocomposites with enhanced visible light photocatalytic activities. J Colloid Interface Sci 448:17–23
40. Di LJ, Yang H, Xian T, Chen XJ (2018) Facile synthesis and enhanced visible-light photocatalytic activity of novel p-Ag_3PO_4/n-$BiFeO_3$ heterojunction composites for dye degradation. Nanoscale Res Lett 13:257
41. Liu WJ, Li C, Ren YJ, Sun XB, Pan W, Li YH, Wang JP, Wang WJ (2016) Carbon dots: surface engineering and applications. J Mater Chem B 4:5772–5788
42. Li HT, Kang ZH, Liu Y, Lee ST (2012) Carbon nanodots: synthesis, properties and applications. J Mater Chem 22:24230–24253
43. De B, Karak N (2017) Recent progress in carbon dot-metal based nanohybrids for photochemical and electrochemical applications. J Mater Chem A 5:1826–1859
44. Lim SY, Shen W, Gao ZQ (2015) Carbon quantum dots and their applications. Chem Soc Rev 44:362–381
45. Wang R, Lu KQ, Tang ZR, Xu YJ (2017) Recent progress in carbon quantumdots: synthesis, properties and applications in photocatalysis. J Mater Chem A 5:3717–3734
46. Zhang HC, Huang H, Ming H, Li HT, Zhang LL, Liu Y, Kang ZH (2012) Carbon quantum dots/Ag_3PO_4 complex photocatalysts with enhanced

photocatalytic activity and stability under visible light. J Mater Chem 22: 10501–10506
47. Wang S, Li LP, Zhu ZH, Zhao ML, Zhang LM, Zhang NN, Wu QN, Wang XY, Li GS (2019) Remarkable improvement in photocatalytic performance for tannery wastewater processing via SnS_2 modified with N-doped carbon quantum dots: synthesis, characterization, and 4-nitrophenol-aided Cr(VI) photoreduction. Small 2019:1804515
48. Huang WY, Wang SH, Zhou Q, Liu X, Chen XR, Yang K, Yu CL, Li D (2017) Constructing novel ternary composites of carbon quantum dots/Bi_2MoO_6/graphitic nanofibers with tunable band structure and boosted photocatalytic activity. Sep Purif Technol 217:195–205
49. Sharma S, Mehta SK, Ibhadon AO, Kansal SK (2019) Fabrication of novel carbon quantum dots modified bismuth oxide (a-Bi_2O_3/C-dots): material properties and catalytic applications. J Colloid Interface Sci 533:227–237
50. Zhang YF, Park M, Kim HY, Ding B, Park SJ (2017) A facile ultrasonic-assisted fabrication of nitrogen-doped carbon dots/BiOBr up-conversion nanocomposites for visible light photocatalytic enhancements. Scientific Reports 7:45086
51. Zhang HC, Ming H, Lian SY, Huang H, Li HT, Zhang LL, Liu Y, Kang ZH, Lee ST (2011) Fe_2O_3/carbon quantum dots complex photocatalysts and their enhanced photocatalytic activity under visible light. Dalton Trans 40:10822–10825
52. Di J, Xia JX, Ji MX, Wang B, Yin S, Zhang Q, Chen ZG, Li HM (2015) Carbon quantum dots modified BiOCl ultrathin nanosheets with enhanced molecular oxygen activation ability for broad spectrum photocatalytic properties and mechanism insight. ACS Appl Mater Interfaces 7:20111–20123
53. Chen CC, Fan T (2017) Study on carbon quantum dots/$BiFeO_3$ heterostructures and their enhanced photocatalytic activities under visible light irradiation. J Mater Sci Mater Electron 28:10019–10027
54. Gao HJ, Zheng CX, Yang H, Niu XW, Wang SF (2019) Construction of a CQDs/Ag_3PO_4/$BiPO_4$ heterostructure photocatalyst with enhanced photocatalytic degradation of rhodamine B under simulated solar irradiation. Micromachines 10:557
55. Xian T, Yang H, Dai JF, Wei ZQ, Ma JY, Feng WJ (2011) Photocatalytic properties of $BiFeO_3$ nanoparticles with different sizes. Mater Lett 65:1573–1575
56. Zheng CX, Yang H, Cui ZM, Zhang HM, Wang XX (2017) A novel $Bi_4Ti_3O_{12}$/Ag_3PO_4 heterojunction photocatalyst with enhanced photocatalytic performance. Nanoscale Res Lett 12: 608
57. Huang WY, Liu N, Zhang XD, Wu MH, Tang L (2017) Metal organic framework g-C_3N_4/MIL-53(Fe) heterojunctions with enhanced photocatalytic activity for Cr(VI) reduction under visible light. Appl Surf Sci 425: 107-116
58. Xie RY, Zhang LP, Liu HC, Xu H, Zhong Y, Sui XF, Mao ZP (2017) Construction of CQDs-$Bi_{20}TiO_{32}$/PAN electrospun fiber membranes and their photocatalytic activity for isoproturon degradation under visible light. Mater Res Bull 94: 7-14
59. Yan YX, Yang H, Yi Z, Xian T, Li RS, Wang XX (2019) Construction of Ag_2S@$CaTiO_3$ heterojunction photocatalysts for enhanced photocatalytic degradation of dyes. Desalin Water Treat (https://doi.org/10.5004/dwt.2019.24747)
60. Wang YY, Qin F, Yi Z, Chen XF, Zhou ZG, Yang H, Liao X, Tang YJ, Yao WT, Yi YG (2019) Effect of slit width on surface plasmon resonance. Results Phys 15:102711
61. Liang CP, Zhang YB, Yi Z, Chen XF, Zhou ZG, Yang H, Yi Y, Tang YJ, Yao WT, Yi YG (2019) A broadband and polarization-independent metamaterial perfect absorber with monolayer Cr and Ti elliptical disks array. Results Phys 15:102635
62. Yan YX, Yang H, Yi Z, Wang XX, Li RS, Xian T (2019) Evolution of Bi nanowires from BiOBr nanoplates through a $NaBH_4$ reduction method with enhanced photodegradation performance. Environ Eng Sci (https://doi.org/10.1089/ees.2019.0284)
63. Wang SY, Yang H, Wang XX, Feng WJ (2019) Surface disorder engineering of flake-like Bi_2WO_6 crystals for enhanced photocatalytic activity. J Electron Mater 48: 2067-2076
64. Pooladi M, Shokrollahi H, Lavasani SANH, Yang H (2019) Investigation of the structural, magnetic and dielectric properties of Mn-doped $Bi_2Fe_4O_9$ produced by reverse chemical co-precipitation. Mater Chem Phys 229: 39-48
65. Zhang XY, Liu JK, Wang JD, Yang XH (2015) Mass Production, Enhanced Visible Light Photocatalytic Efficiency, and Application of Modified ZnO Nanocrystals by Carbon Dots. Ind Eng Chem Res 54: 1766-1772
66. Yan YX, Yang H, Yi Z, Xian T, Wang XX Direct Z-scheme $CaTiO_3$@BiOBr composite photocatalysts with enhanced photodegradation of dyes. Environ Sci Pollut R (https://doi.org/10.1007/s11356-019-06085-y).
67. Zhao XX, Yang H, Cui ZM, Yi Z, Yu H (2019) Synergistically enhanced photocatalytic performance of $Bi_4Ti_3O_{12}$ nanosheets by Au and Ag nanoparticles. J Mater Sci Mater Electron 30: 13785-13796
68. Ren HT, Ge L, Guo Q, Li L, Hu GK, Li JG (2018) The enhancement of photocatalytic performance of $SrTiO_3$ nanoparticles via combining with carbon quantum dots. RSC Adv 8: 20157-20165
69. Ye YC, Yang H, Zhang HM, Jiang JL A promising (2019) Ag_2CrO_4/$LaFeO_3$ heterojunction photocatalyst applied to photo-Fenton degradation of RhB. Environ Technol (https://doi.org/10.1080/09593330.2018.1538261)

Publisher's Note